The development of a high-performance Ni-superalloy additively manufactured heat pipe

Li, Sheng; Essa, Khamis; Carr, James; Chiwanga, States; Norton, Andrew; Attallah, Moataz

[Link to publication on Research at Birmingham portal](#)

The development of a high-performance Ni-superalloy additively manufactured heat pipe

Sheng Li[1,2] · Khamis Essa[2] · James Carr[3] · States Chiwanga[4] · Andrew Norton[5] ·
Moataz M. Attallah[6]

Abstract Additively manufacturing (AM) has been used to manufacture fine structures with structured/engineered porosity in heat management devices. In this study, laser powder bed fusion (LPBF) was used to manufacture a high-performance Ni-superalloy heat pipe, through tailoring LPBF process parameters to fabricate thin wall and micro-channel. By using novel laser scanning strategies, wick structure heat pipes with maximised surface-area-to-volume ratio, fine features size around 100 μm, and controlled porosity were successfully fabricated. Microscopy and X-ray microtomography (micro-CT) were used to investigate the 3D structure of the void space within the pipe. Wick test results showed that most of the heat pipes made by LPBF had better performance than the conventionally manufactured pipes. This study also investigated the influences of the process parameters on the porosity volume fraction and the feature size. The results showed that LPBF process could fabricate thin structure due to the change of melt pool contact angle. The relationship between process parameters and bead size reported in this study could help design and manufacture heat pipe with complex fine structure.

✉ Moataz M. Attallah
m.m.attallah@bham.ac.uk

1   School of Electromechanical Engineering, Guangdong
    University of Technology, Guangzhou 510006,
    People's Republic of China

2   School of Engineering, University of Birmingham,
    Edgbaston, Birmingham B15 2TT, UK

3   Henry Moseley X-ray Imaging Facility, Henry Royce
    Institute for Advanced Materials, Department of Materials,
    University of Manchester, Manchester M13 9PL, UK

4   European Thermodynamics Ltd, 8 Priory Business Park,
    Wistow Road, Kibworth, Leicestershire LE8 0RX, UK

5   Rolls-Royce plc, P.O. Box 31, Derby DE24 8BJ, UK

6   School of Metallurgy and Materials, University
    of Birmingham, Edgbaston, Birmingham B15 2TT, UK

1 Introduction

Heat pipes are widely used in mechanical, electrical and energy industries as a thermal management device transferring latent heat through evaporation and condensation [1–4]. Most current heat pipes have simple porous structure or simple groove geometry structure, as they are manufactured powder sintering or extrusion [2, 5–7]. These manufacturing techniques have very limited control on the geometry and size of pores, hence the performance of porous wick itself has not been significantly improved in the last few decades. In recent years, the development of additively manufacturing (AM), as a method to produce net-shape or near-net-shape components, has introduced a game changing manufacturing process to high performance design with more freedom [8–10]. Laser powder bed fusion (LPBF, also known as selective laser melting), as a widely used AM technique, can reliably produce pores from a few hundred microns to a few millimetres and complex structures, which are impossible to manufacture using traditional methods [11–13]. Previous studies used LPBF to build lattice (mesh) and porous structures, which attracted significant interest due to their potential applications in shock absorption, thermal management and medical implants [14–17].

So far there are a few studies on LPBFed heat pipes. Ameli et al. [18] studied the permeability of aluminium wick heat pipe made with diamond shape lattice wick by LPBF process and some manufacturing defects were found in the lattice. Ibrahim et al. [19] and Thompson et al. [20] fabricated a Ti6Al4V oscillating heat pipe with 1.5 mm internal channel via additively manufacturing. Jafari et al. [21] compared the conventional heat pipes and additively manufactured 316L stainless steel heat pipes with strut size around 200 μm. However, these studies focused on wick performance comparing to traditional heat pipes rather than improving the wick performance by exploring the process parameters.

It is well known in AM community that the process parameters for block materials and fine structure are different [13, 22]. Making the wick structure as close to the design as possible is essential before studying the performance. Therefore, alternative approaches must be devised for process optimisation when building fine and thin-walled structures for heat pipes. Some studies have fabricated fine lattice structures, however, the influences of the process parameters on the strut size and morphology were unclear [17, 23–27]. ElSayed et al. [28] analysed the influence of the laser heat input, expressed within the form of the energy density, on the porosity, elastic modulus and surface roughness of Ti6Al4V

lattices. Nonetheless, the energy density failed to establish direct correlations with the strut size control. Valdez et al. [29] used LPBF to fabricate porous IN718 but failed to find a clear relationship between process parameters and pore sizes. Recently, Salem et al. [30] investigated the mechanisms of defect formation during LPBF of Ti6Al4V lattices, highlighting the complexities of the relationship between the process parameters and the defect type or strut size. The single bead method, which uses a single laser line scanned on the substrate, is an effective way to study the influences of laser parameters on bead size (feature size) [31].

On the other hand, the wick structure with feature size below 150 μm has not been reported, exploring the minimum feature size of LPBFed will help heat pipe researchers to design LPBFed heat pipes. Searle et al. [32] successfully fabricated heat pipes with a fine diameter of around 600 μm. Zhang et al. [33] fabricated a heat exchanger with microchannels around 220 μm size. A novel method, combining the single bead fabrication and scan strategy design, was proposed and investigated in this study.

This study aims to investigate the limit of thin structure fabrication in LPBF and reveal the relationship among processing parameters, structure size and wick performance. INCONEL® 718 alloy (commonly referred to as IN718) heat pipes were produced in this study as an example, demonstrating the AM of a high temperature heat pipe operates at 650°C. By using the single bead method and novel laser scanning strategy, a series of IN718 heat pipes with controlled porous inner surfaces were fabricated. The performance of LPBFed heat pipes was compared with a traditionally manufactured heat pipe via wick test and thermal imaging. The inner structure of LPBFed heat pipes was investigated by microscopy and CT scan.

2 Materials and experimental method

2.1 LPBF

IN718 gas atomised powder (supplied by LPW Technology, Ltd.) with particle sizes between15 μm and 53 μm was processed using a Concept Laser M2 cusing LPBF platform with a 400 W fibre laser. The powder particle size distribution was detemind by SympaTEC laser diffraction particle size analyser. The D_{10}, D_{50} and D_{90} value were 14.42 μm, 28.11 μm and 42.40 μm, respectively. The machine equpied a Gaussian energy distributed laser beam with a spot size between 67 μm and 73 μm and within 80–400 W power range. The laser spot size is 67 μm at 80–100 W, and 71–73 μm when the power is higher than 200 W. Hence we consider the diameter of laser spot size as a constant value (70 ± 3 μm) in this study. The nominal layer thickness was fixed at 30 μm in this study. Regarding the build orientation, the

X-axis is the powder re-coating and argon gas flow direction; the *Y*-axis is the planar normal to the *X*-direction on the substrate surface, whilst the *Z*-axis is the building direction. All samples were produced on a mild steel substrate under a flowing argon atmosphere controlled to lower than 0.01% O_2 and subsequently removed from the substrate using a GF Agie Charmilles CUT 20 electric discharge machining (EDM) machine.

To represent the heat input, energy density concept is conventionally used [16, 34], which gives an equivalent heat input value based on the process parameters including laser power (*P*), scan speed (*v*), scan or hatch spacing (*h*) and layer thickness (*T*). This can be presented as

$$E_V = \frac{P}{v \times h \times T}, \qquad (1)$$

$$E_A = \frac{P}{v \times h}, \qquad (2)$$

$$E_L = \frac{P}{v}, \qquad (3)$$

where E_v is the nominal volume energy density, E_A the nominal area energy density, E_L the nomical linear energy density.

Although volumetric energy density (VED) with laser beam diameter included is widely used in many studies [35],

Low energy strategy

Mesh strategy

Grooved strategy

Fig. 1 Schematic illustrations for the different geometries

Table 1 Coupon geometry and parameters fabricated by different strategies, coupon width *w*, coupon height *l*, external wall thickness *c* and coupon diameter Ø

Scan strategy	Coupon size ($w \times l \times c$) or ($Ø \times l \times c$)	Power/W	Scan speed/(mm·s^{-1})	Hatch spacing/mm
Low energy	5 mm ×10 mm ×1 mm	80–125	1 000–4 200	0.112 5–0.3
Mesh	2.5 mm × 2.5 mm × 0.5 mm	80–300	1 000–3 500	0.15–0.3
Grooved	10 mm × 10 mm × 1 mm (tooth interval 0.15 mm)	80–200	1 000–3 500	0.015–0.03

it is not used in this study as the laser beam diameter is almost constant in this study. To study the influences of the process parameters on the porosity, coupons with opened top and bottom ends were built. Inside the coupons, different scanning strategies were used to create and optimise porous structures, which are the low energy, mesh and grooved-strategies (see Fig. 1). The geometry and parameter information of these coupons are listed in Table 1. The low energy scanning strategy used a raster scanning (simple scanning) strategy, rotated 90° between the subsequent powder layers, with a large hatch spacing (varying from 0.112 5 mm to 0.3 mm) and relatively low power (within 80–125 W range). Since only one direction is scanned across each layer and large hatch spacing is used, the nominal powder layer thickness of the most area (apart from the cross points of the sacn paths between subsequent layers) in this strategy is doubled (i.e., 60 μm), as shown in Fig. 1. Therefore, this strategy has a significantly lower VED input than other strategies. This approach aims to create a highly porous mesh, with the large hatch space resulting in non-overlapping laser tracks, creating a mesh-like structure. Within the mesh strategy, the laser beam scansfully hatched patterns in each layer to create a regular square mesh structure with the designed mesh size. A constant scan spacing was used for each direction and layer, assessing scan spacing within the range of 0.15–0.3 mm and power ranging 80–300 W. The mesh structure strategy coupons were 2.5 mm × 2.5 mm × 5 mm mesh cubes, surrounded by a 0.5 mm thick wall. The scan spacing for these cubes was fixed at either 0.24 mm or 0.3 mm. Lastly, the grooved-strategy was used in pipes with a circular cross section to create a pipe with internal teeth-like features. Although this differed from the two previous designs, where a uniform porous structure was used to maximise heat losses, the dense teeth-like structure was also known to deliver similar performances [36]. The grooved-structure used 0.15 mm long and 0.15 mm spaced teeth which were uniformly distributed on the internal surface along with the cylinder height. A round hollow cylindrical pipe with a 1 mm wall thickness was fabricated as the external shell. The teeth design aimed at maximising the surface area and reducing the performance difference between vertical direction and horizontal direction. The scan strategy for the teeth was a simple non-rotating scan parallel to the long axis of the teeth (perpendicular to the pipe inner surface). Different standard tessellation language (STL) files were used for the teeth and the hollow pipe, ensuring that the scanning strategies would not interfere with one another. The STL files were carefully positioned on the substrate to ensure a good overlap between the teeth and the external shell. This grooved-structure could be used in both horizontal and vertical directions.

2.2 Characterisation

Sections of the porous structures were extracted for microscopic examination. The cut sections were mechanically ground and diamond-polished to a 0.3 μm oxide solution finish. The samples were then immersed in ethanol and ultrasonically cleaned for one hour to remove the loose powder. To quantify the porosity fraction, pore size and width of the mesh beads, images were taken using a ZEISS optical microscope and an HITACHI TM3000 scanning electron microscope (SEM) before subsequent analysis using ImageJ software. A Nikon custom bay micro-CT system was used to assess the internal 3D structure of the void space between the inner and outer walls of the heat pipe. Acquisition parameters can be found in Table 2.

Micro-CT was also used to study the influences of thermal cycleson structural integrity. The thermal cycles were as follows: ramp up to 600 °C at 5 °C/min, then held for 1 h, followed by 55 min air cooling. Each sample was built vertically and was thermal cycled 50 times before another CT scan. Each sample, with a length of 130 mm, was scanned in two different locations near the top and bottom of the shaft with each scan comprising 20 mm of the shaft length.

Table 2 Acquisition settings used for the micro-CT

	Value
Accelerating voltage/kV	130
Tube current/μA	50
Target material	Tungsten (W)
Filter	2.5 mm copper (Cu)
Reconstructed voxel size/μm	10
Exposure time/s	4
Number of projections	3 142

The micro-CT provides 3D volume renders and non-destructive virtual cross sections through the part. In addition, the cross-sectional area of the void space between the inner and outer walls was segmented using a water shed segmentation algorithm. This allowed for quantification of the void space which could be used as a metric for determining changes non-destructively.

2.3 Assessment of the capillary performance

The capillary performance was measured by performing in-situ thermal measurements. A ThermaCAM SC640 infrared thermal imaging camera was used to observe 18 °C deionised water wicking from the bottom of the heat pipe. The heat pipes were cut into two pieces along the vertical section and a thermal camera was used to trace the temperature of the heat pipe, as shown in Fig. 2. Using an acquisition rate of 24 frames per second, the wicking speed (to achieve 18 °C at the top of the pipe) was calculated. A copper heat pipe made by powder sintering was a reference sample.

3 Results and discussion

3.1 Low energy strategy

SEM micrographs, taken from the top of the builds (see Fig. 3), show the morphology of the pores. The samples were manufactured with three levels of power (named as low, medium and high powers), as shown in Table 1. As the power used in low energy strategy was relative lower than those in other strategy, the porosity was mainly altered by changing hatch spacing. The increasing hatch spacing results in more defined channels when using medium power (see Figs. 3a, b). A comparison of the higher power to the medium power conditions shows the higher power leads to a better pattern definition, compared with more smudging of

the channels within the medium power sample. The samples in Figs. 3a, b had a bead width of 100–150 μm, increasing to 300 μm within the regions where balling (poor melt wetting) is observed [37]. Conversely, the samples built using high power (e.g., Figs. 3c, d), had a thinner bead, with a typical bead width of lower than 200 μm. Comparing the samples built using different E_L and the same hatch spacing (e.g., Figs. 3a, c), the lower E_L condition (see Fig. 3c) had a more defined bead, due to narrower, yet stable, melt pool. The higher E_L condition (see Fig. 3a), whose wider melt pool was due to balling and its instability, led to discontinuities within the melted bead and the smudging of the channels by partially melted powders. Lastly, when comparing the samples built using different hatch spacings (e.g., Figs. 3c, d), the pore sizes become relatively larger, with a mean pore size of 0.030 mm^2 (61 μm equivalent diameter) in Fig. 3c compared with 0.041 mm^2 (71 μm equivalent diameter) in Fig. 3d.

By plotting E_A against the area fraction of porosity (see Fig. 4a), the porosity fraction reduces almost linearly with an increase in E_A. A similar trend is reported within the literature for LPBF of Ti-alloys and Ni-superalloys [16, 25, 38, 39], showing a consolidation threshold exists when the energy density becomes sufficient to cause full consolidation of the material. The threshold is typically larger than 1.5 J/mm^2 for Ni-superalloys [40]. As such, it was expected that the investigated parameters would create a porous structure. There is some scatter within the data, with less linearity within the E_A versus porosity relationships, for the samples built using low power parameters. It is also found that the highest porosity condition is achieved by the medium power parameter, which is caused by the combination of different hatch spacings and nonlinear changes of bead width. Bertoli et al. [35] studied the bead width and melt pool depth of 316L SS on a single layer deposition condition. The bead width on a laser fabricated surface has not been studied yet. Therefore, further study on the influence of E_L on the
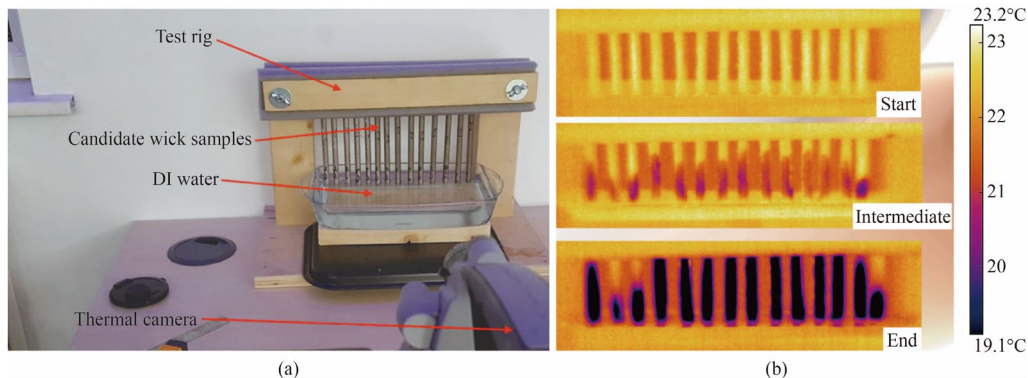

Fig. 2 Assessment of the capillary wicking action **a** the test setup with cold deionised water and the thermal camera, and **b** thermal imaging still shots at the start, midway and end of the test
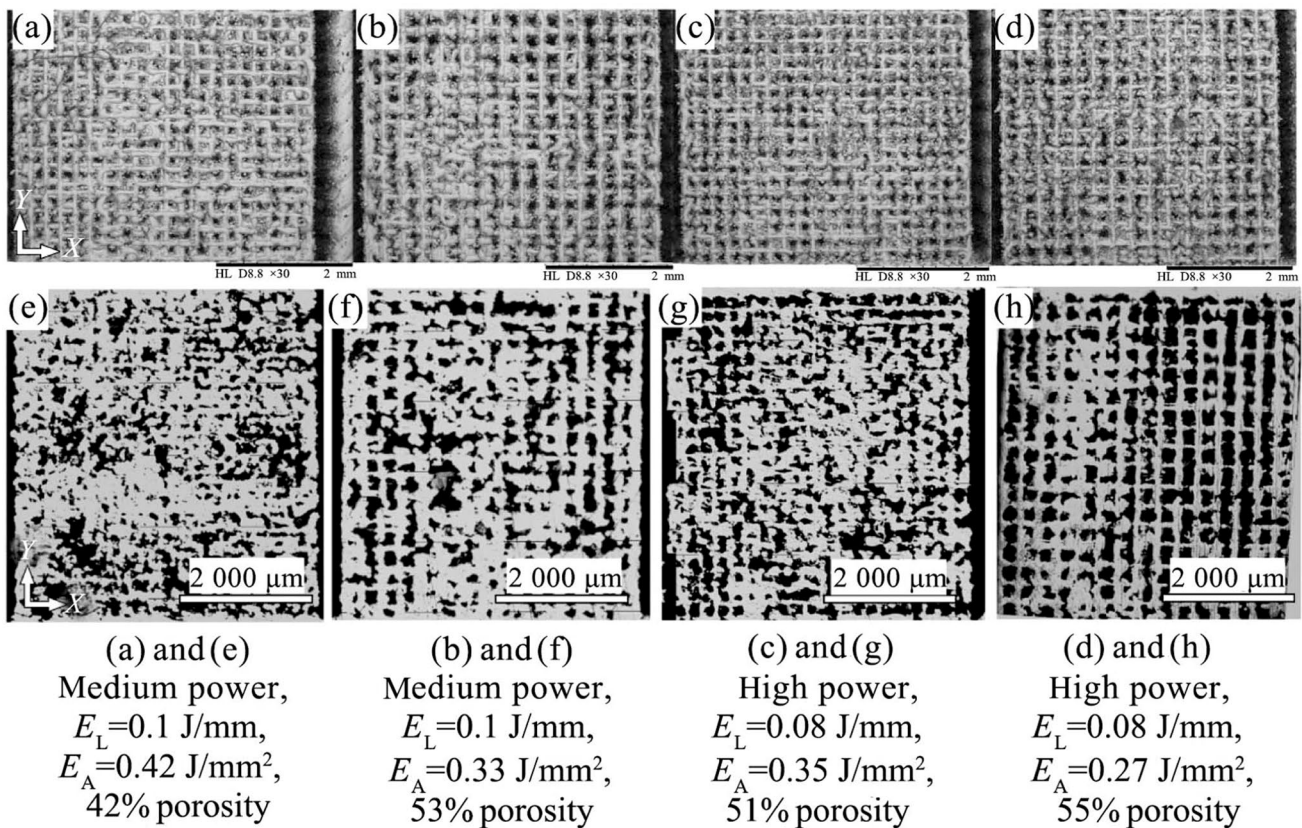
(a) and (e)
Medium power,
E_L=0.1 J/mm,
E_A=0.42 J/mm²,
42% porosity

(b) and (f)
Medium power,
E_L=0.1 J/mm,
E_A=0.33 J/mm²,
53% porosity

(c) and (g)
High power,
E_L=0.08 J/mm,
E_A=0.35 J/mm²,
51% porosity

(d) and (h)
High power,
E_L=0.08 J/mm,
E_A=0.27 J/mm²,
55% porosity

Fig. 3 SEM micrographs for the top surface and horizontal section of the lower energy strategy samples

bead width is necessary. Only six samples built using low power were successfully fabricated, creating a structurally sound build, out of the 32 samples built at this power. The low power was insufficient to fully melt the powder, instead it induced the balling effect [41], which could lead to discontinuities within the laser tracks. Valdez et al. [29] also reported sintered powder and discontinuous bead in LPBFed IN718 mesh structures. The number of structurally sound samples increased with increasing laser power. It must be emphasised that uniformed porous structures were only possible through the use of a large hatch spacing, alongside the lower energy density range to avoid overlap between the neighbouring tracks.

Previous analysis using E_A considered all parameters [29]. However, to deconvolute the impact of the hatch spacing, it is beneficial to look into the relationship between E_L and the hatch spacing, as shown in Fig. 4b. The combination of E_L lower than 0.1 J/mm and hatch spacing within 0.18–0.3 mm range is required to achieve the target of 50% porosity, while keeping the power lower than the high power level. The energy density affects both the melt flow and the degree of wetting, which may lead to balling by insufficient wetting and discontinuities beads when the energy density is low. Meanwhile, if the energy density is too high,

the process generates thicker beads which reduce the gaps between neighbouring tracks, creating a denser material. On the lower energy density end, balling generates non-uniformed porosity, resulting in smudging of holes and irregular mesh structures, while the higher energy density will block the mesh pores by densifying the material. Similarly, the hatch spacing must be chosen to balance the energy density effects to achieve the target density. Using Fig. 4, the optimum processing window (50% porosity) is when E_A is within 0.3–0.4 J/mm² range, with the process parameters following this relation

$$h - \frac{20P}{13\nu} = \frac{9}{130}, \quad 80 \leq P \leq 125, \quad 200 \leq h \times \nu \leq 416.67,$$
(4)

where the laser beam is considered as a constant beam with average beam diameter of 70 ± 3 μm. When comparing the results of this strategy with the findings of later strategies, it is not going to be straightforward from an energy density viewpoint. Within the lower energy strategies, the same laser tracks are repeated every two powder layers, meaning the nominallayer thickness is 60 μm. This also affects the integrity of the structure, since the melt pool in each track
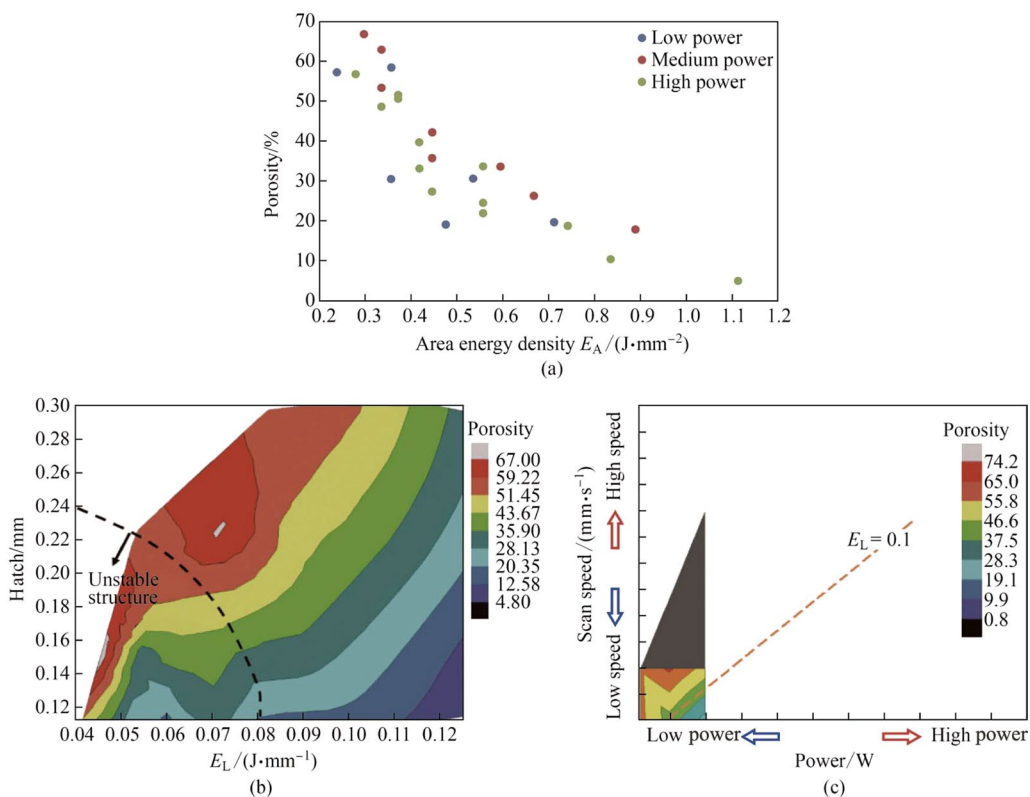
Fig. 4 Porosity area fraction versus **a** the area energy density, **b** linear energy density, **c** power and scan speed (with 0.3 mm h) within the lower energy density builds (the black dash line indicates the unstable parameter area)
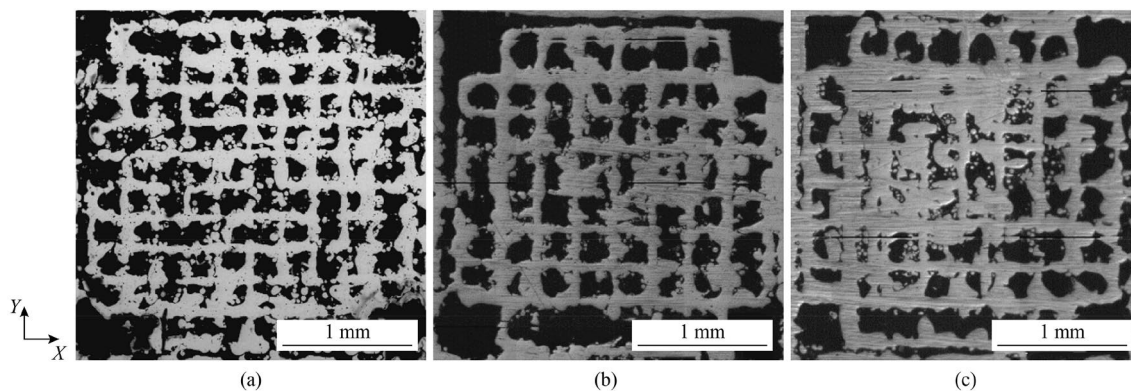

Fig. 5 Mesh strategy samples produced by **a** low power, $E_L = 0.064$ J/mm, $E_A = 0.27$ J/mm^2, **b** medium power, $E_L = 0.067$ J/mm, $E_A = 0.22$ J/mm^2, and **c** high power, $E_L = 0.056$ J/mm, $E_A = 0.19$ J/mm^2

must be deep enough to weld the subsequent layers together, especially each n and $n+2$ layers.

Regarding the build quality, partially melted/sintered powder was found on the sample surface. The size of the powder was between 10 μm and 50 μm, the size range of as-received powder, suggesting that lower energy reduced the tendency for consolidation at the melt pool edge. Instead, powers partially stuck to the edge of the melt pool, which

had less energy due to the surface tension of the melt. It is known that evaporation and plasma recoil pressure during LPBF, which may force the powders to move towards the laser tracks, depend on the process parameters, causing a powder spreading known "denudation" [42]. No strong metallurgical bonding formed between the melt track and the surrounding powders, allowing for them to be removed by sandblasting or a similar technology.

3.2 Mesh strategy

SEM micrographs, taken from the *XY* section of the mesh strategy samples, showed defined square pores at lower powers, with more partially melted powder particles sticking on the structure athigher powers (see Fig. 5). Overall, samples built with higher laser power had more partially melted/sintered particles attached to the beads, with less defined mesh structures. This result highlights the impact of scanning strategies in controlling the amount of heat. As aforementioned, the nominal layer thickness within the low energy strategy is equivalent to half the nominal volumetric energy within the mesh strategy, should the same laser parameters be used. As such, balling was less prominent within the low power mesh conditions (see Fig. 5a). Conversely, the higher power conditions resulted in more powders sticking to the melt bead and consuming surrounding powders (see Fig. 5c). The medium power condition produced stable thin wall around 100 μm, as shown in Fig. 5b. The lower energy and mesh strategies were able to deposit thin walled structures in this study at energy levels reported as not printable parameters in other studies [38].

In the mesh strategy, two scan spacing levels were used, while maintaining a generally low E_L to avoid full or near consolidation of the mesh, due to the creation of thicker beads when a higher E_L is used. The parameters covered the most power used in LPBF (up to 350 W). Figure 6a shows the influence of the laser power and scan speed on the laser track (bead) width within the mesh. The bead width linearly increased with the increase in power and decrease inscan speed. At higher powers, the bead width grows slower at higher scan speeds. The bead width grows higher than hatch spacing when the E_L exceeds 0.13 J/mm. Within conditions sharing the same E_L, the bead width slightly increases with the increase in laser power, especially when the power higher than the high power level. This behaviour also holds from a

porosity viewpoint (see Fig. 6b). Due to the higher energy input, the melt pool becomes hotter and wider, pulling more powder particles by surface tension and recoil, which leads to further partial melt and sintering[42]. In general, the structure produced by low energy and mesh strategy shows the ability of fabricating thin structure around 100 μm in width, which is half the size of micro-channel reported in the literature (220–670 μm) [18, 33, 43]. Comparing low energy strategy to mesh strategy with the same parameters (Fig. 4c versus Fig. 6b), low energy strategy has higher porosity.

By plotting the bead width (*D*) against E_L (see Fig. 7), a relation between the bead width and $E_L = P/v$ was developed

$$D = A(P) \times \ln E_L + B(P), \tag{5}$$

where *P* is laser power, $A = -0.026P + 58.38$ and $B = 0.079P + 214.39$. The R^2 value of the model is from 0.972 to 0.998, indicating good accuracy, as shown in Fig. 7. This indicates that the laser power has a strong influence on melt pool size, as the energy input of laser and number of reflections increases with increasing laser power when $80\,\text{W} \leq P \leq 300$ W. The high laser power enables more reflections within the powder bed, allowing more powder to absorb the laser energy and therefore creat a larger melt pool [44]. Dilip et al. [25] also reported the melt pool width in LPBF of Ti6Al4V followed a logarithmic relation to both the laser power and scan speed. The influence of the power on the bead width is less significant for lower power parameters (comparing low power to high power in Fig. 7). It also shows that the influence of power is stronger in higher E_L parameters (low scan speed) comparing to low E_L parameters. Comparing with the other studies using single layer single bead method [35], our multi-layer single bead study shows that the laser power has stronger impact on the bead width (increased from 90 μm to 120 μm, when power increased from 80 W to 300 W). This could be associated with the increased laser energy at
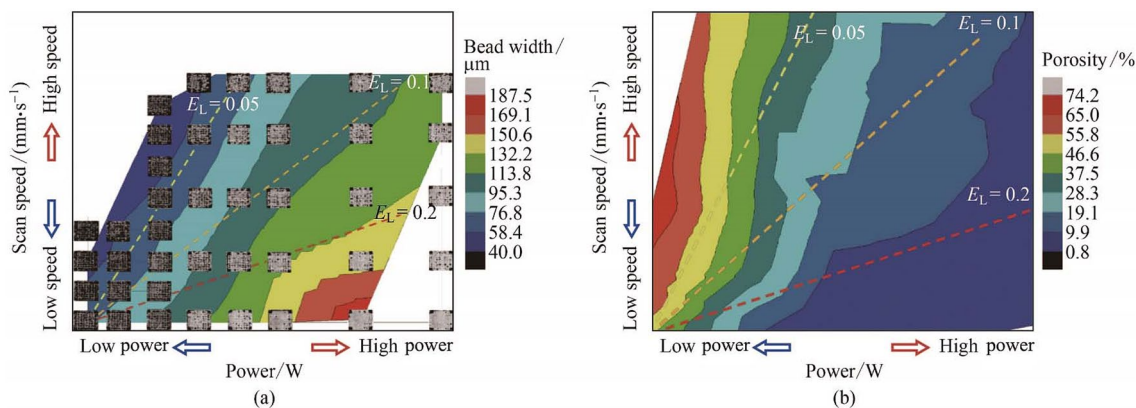

Fig. 6 Process maps for the mesh structure showing **a** the influence of the laser power and scan speed on bead width, and **b** the influence of the laser power and scan speed on porosity
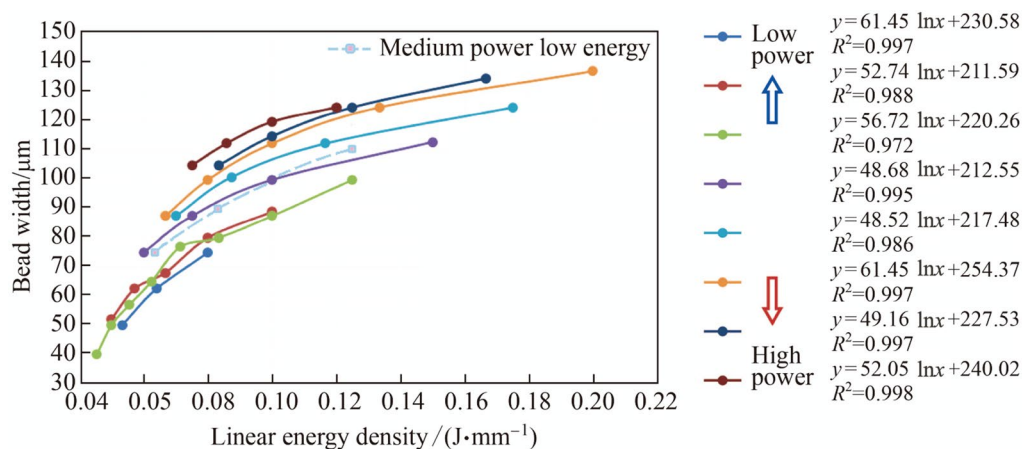
Fig. 7 Variation in bead width with the linear energy density in mesh strategy samples and medium power low energy strategy samples

higher powers, as well as the reflection and absorptivity of powder [44, 45]. The higher power provided more energy to the laser, allowing more reflections between powder particles in the powder bed. The low energy strategy samples built by medium power (the same power as the green line of mesh strategy) has slightly higher bead width due to the thicker nomial powder layer comparing to the mesh strategy samples.

3.3 Grooved-strategy

The low energy and mesh studies show thin wall around 100 μm width is printable in LPBF. Previous works suggested that horizontally-built structures were affected by over-melting and a lack of support at the base surface [16]. A few grooved structure heat pipes with the 100–150 μm width teeth perpendicularly positioned to the pipe inner wall were fabricated in both vertical and horizontal directions, and the geometrical integrity of this structure is studied. To reduce the influences of the laser scanning direction on teeth geometry, the laser scan path is controlled, meaning it is always parallel to the longitude direction of the teeth. A number of optimum parameters were selected base on the low energy and mesh studies to maintain a 120 μm teeth interval distance at the tips. Among the investigated parameters, the $E_L = 0.064$ J/mm condition resulted in a smaller teeth width (100 μm), with a uniformed 100 μm spacing between the teeth.

The horizontally-built grooved-structures have good geometrical integrity, at both the bottom and the top of the pipe, as shown in Figs. 8a, b. The geometry accuracy of grooved-strategies was strongly affected by the build direction. The length of the top teeth is shorter, due to a lack of support within the first few layers and an over melting from the pipe wall, but the gap between the teeth remains the correct size. The geometry of the side teeth, which is perpendicular to the

build direction, is affected by over melting and a lack of support, as shown in Fig. 8c. Partially-melted particles between the horizontal teeth (see Fig. 8d) have a similar structure to heat pipe with sintered-grooved composite wick reported by Li et al. [46], which showed good performance. In general, low E_L benefits the fine structure fabrication, which ensures a reasonable gap between the teeth.

The non-uniform morphology among the bottom, middle and top surface could be overcome by manipulating the building orientation and using gradient process parameters. The morphology of the top teeth could be improved by tilting the samples 45° to the building direction. On the other hand, using a lower energy process parameters for the mid-diameter sidewall and the top area could also reduce the over-melting and partially melting of the powders.

3.4 Micro-CT

According to the aforementioned results, three samples with 50% porosity were fabricated for micro-CT study. The parameters and strategy for these samples were medium power low energy strategy sample (see Figs. 3b, f), medium power mesh strategy sample (see Fig. 5b), and low power grooved strategy sample (see Fig. 8), respectively. Sections cut from the top and the bottom of the vertically built heat pipe were analysed using micro-CT. The grooved-structure with 1 mm teeth length and 150 μm spacing is shown in Fig. 9a, where limited powder sintering on the groove surface is found. The vertical builds showed a greater uniformity within the teeth size and the distance between them. Nonetheless, a continuous groove channel was built, as shown in Fig. 9b.

Figures 10 and 11 shows the calculated mean cross-section of void space and deviation values of the LPBFed heat pipes base on CT scaned segmentations. It is found that the structures are uniform in both simple structure and
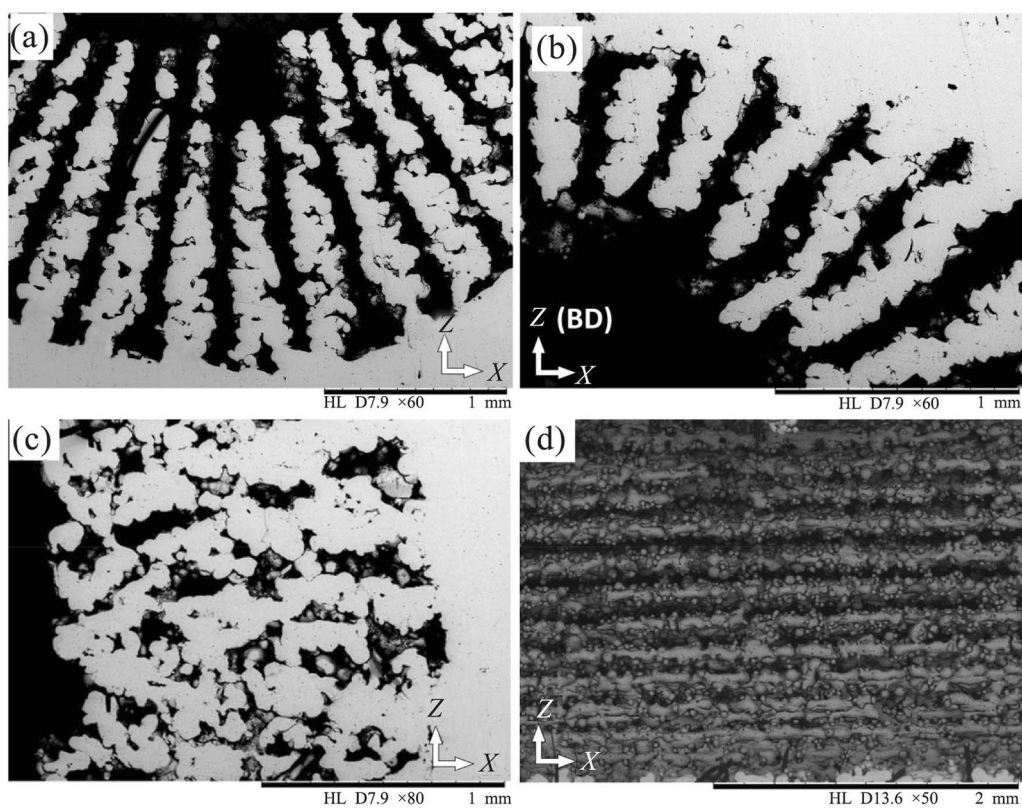
Fig. 8 SEM micrographs for the horizontally built grooved-structures **a** the bottom of the tube with 100–150 µm gap between the teeth, **b** the top of the pipe, **c** the mid-diameter side of the tube, and **d** the side view
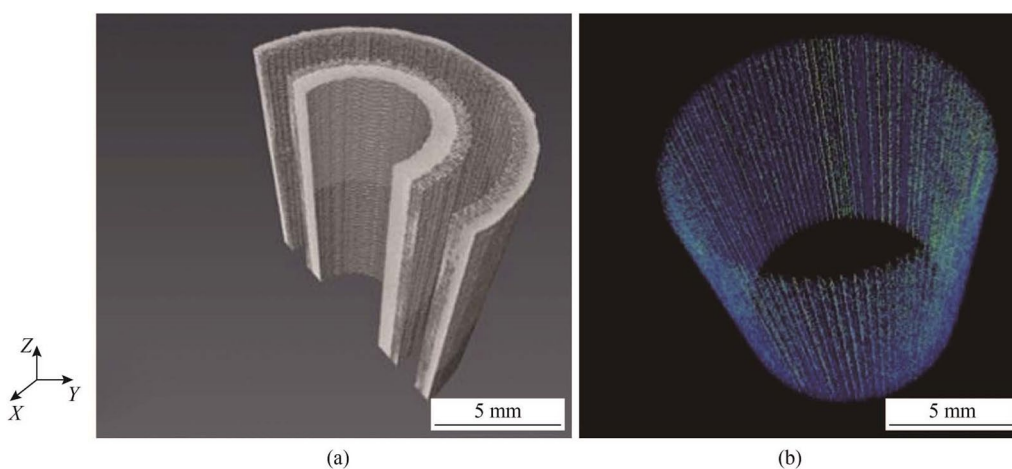

Fig. 9 Micro-CT 3D models showing **a** the uniformity of the internal surface of the heat pipe and **b** the continuity of the grove structures throughout the built height

grooved-structure samples, while the mesh structure had higher variation (about 11%). The cross-section area in the grooved-structure has the lowest deviation as the structure is uniform along the build direction. The cross section of the mesh structure, however, has the highest deviation among

three strategies due to reducing heat transfer and increasing heat accumulation at higher building height. These prompt the balling effect and partial melt powder.

In addition to the volume renderings and skeletonized structures that can be generated using the reconstructed
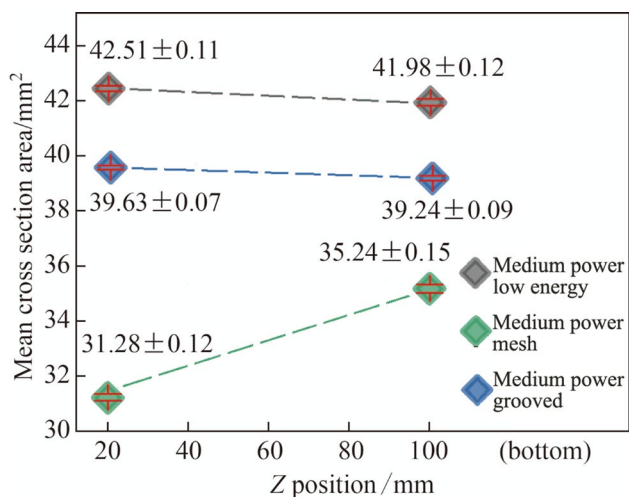
slices (for example, Fig. 9), more intuitive 2D visualizations can be produced. These "virtual cross-sections" present a plane through the sample and provide a non-destructive means for assessing the structure of the heat pipe as shown in Fig. 11. The samples were scanned at as-fabricated condition (see Figs. 11 a, c), and then scanned after 50 thermal cycles (see Figs. 11b, d) to investigate the thermal cycle stability of the structure. There is no obvious change of cross-section area after thermal cycles, which indicates that the samples are stable.

3.5 Bead formation and melt pool stability

The melt pool is considered as a liquid cylinder when studying its stability. One of the common defects in LPBF is that the unstable melt pool breaks into droplets [24, 38]. The Plateau-Rayleigh instability contributes to this unstable status when higher scan speeds are applied [38]. Yadroitsev et al. [23] proposed that the stability of liquid was related to the contact angle Φ (between liquid cylinder and substrate), the diameter of molten pool (D), and molten pool length (L). The melt pool is stable regardless of its dimension when contact angle $\Phi < \pi/2$. Otherwise, the stable condition is

$$\frac{\pi D}{L} > \sqrt{\frac{2}{3}}. \tag{6}$$

As illustrated in Fig. 12a, the melt pool on the flat surface could have $\Phi > \pi/2$, due to surface tension and lower power inputs. This well represents the reality of the single bead, and single layer condition [23]. During the thin wall or lattice structures fabrication in LPBF, the top convex surface of the previous layer is close to a semi-cylinder, which means that the contact angle between the melt pool and solid could be less than $\pi/2$ (see Fig. 12b).Therefore, the melt pool is more stable when producing a thin wall structure than a solid block. Jasper and Anand [47] reported on reducing contact angle between liquid and convex surface, with the reduction insurface radius. As such, the melt pool on the convex surface, when producing thinner structures, has better stability than the melt pool on the flat surface. In the axial direction, the melt pool is unstable if the D/L ratio is less than 0.26 (see Eq. (6)). Thus, the higher the scan speed or the lower
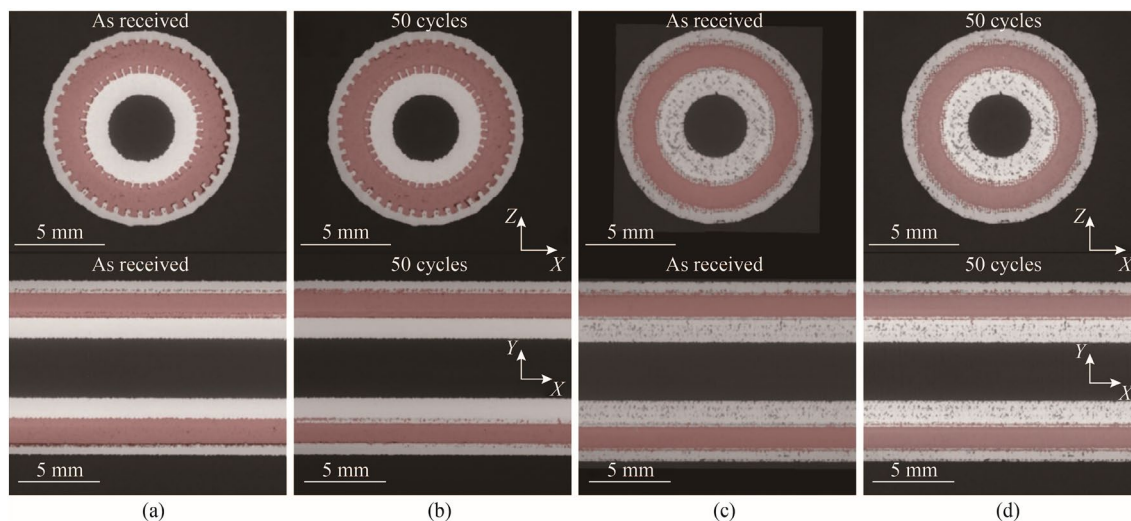

Fig. 11 Virtual cross-sections through vertical built sample **a** grooved-structure in as-fabricated condition, **b** grooved-structure after 50 thermal cycles, **c** mesh structure as-fabricated condition, and **d** mesh structure after 50 thermal cycles (the red portion of the image represents the result of the watershed segmentation)
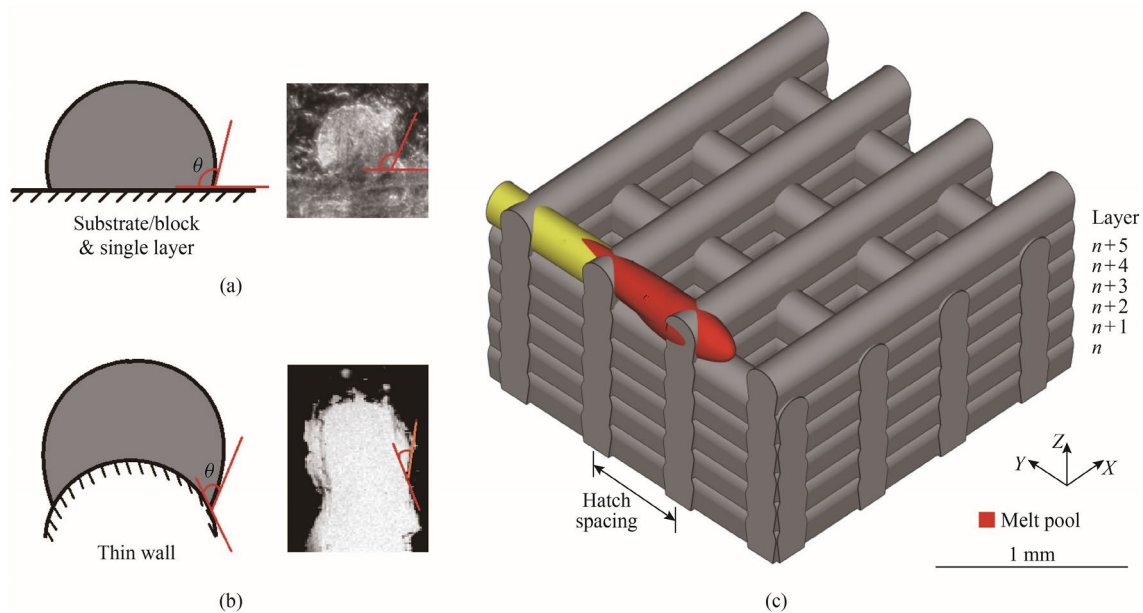
Fig. 12 Schematic drawing of the melt pool during LPBF process when producing different structures **a** for melt pool on substrate or block sample with a relatively flat surface, **b** for melt pool on thin structures with a curved surface ,and **c** more solid area (the red colour is the melt pool, with the yellow and grey the solidified beads)

the laser power is, the lower the *D/L* ratio is, meaning the melt pool is less stable. In this study, it is assumed the melt pool diameter (*D*) is the same as track/bead width, regardless of shrinkage and morphology variations during solidification. According to Eq. (6), the maximum stable melt pool length of printable parameters with lower energy strategies is between 384.6 μm and 576.9 μm. The maximum stable melt pool length of printable parameters with mesh strategy is between 154 μm and 530 μm.

Furthermore, the geometry of mesh structure, which are thin walls perpendicular to each other, also helps stabilise the melt pool by providing more contact surfaces. The periodically solid walls could stabilise the liquid via surface tension and higher cooling rates on solids, shortening the melt pool length, as shown in Fig. 12c. Most conditions in this study could have melt pool lengths larger than the distance between the thin walls. Thus, the thin wall mesh structure has a broader processing window than lower energy strategies, and the mesh strategy sample has less porosity comparing the low energy one with the same parameters (Fig. 6b versus Fig. 4c).

From the study above, we found that the stable melt pool conditions of the first layer of fine structure (flat surface) and the later layers (curved surface) were different. This is one of the reasons that significant difference is often found between the optimised processing parameter of fine structure and block structure in LPBF. Hence, we propose the process parameter of the first layer of the fine structure should be different to the later layers. The first layer should be fabricated

by a high E_L parameter to create a stable wide bead with cruved surface, which improve the stability of the melt pool. By gradually reducing the energy input of the initial layers could create a better fabricating surface for the fine structure and improve the melt pool stability.

3.6 Wick test

The wick performance of the different scanning strategies and the manufacturing parameters was measured using the response time and height of wicking, as per the test described in Sect. 3.3. As shown in Fig. 13, a number of the LPBF IN718 heat pipes demonstrated a good wick performance, compared with the reference Cu heat pipe made from pre-sintered powders, as measured using the response time. The response time was calculated using camera video record from 5 mm wick height to the maximum wick height and fit to first order respond as equation below

$$H_{\text{wick}} = H_{\text{wick-max}}\left(1 - e^{\frac{-t}{\tau}}\right), \tag{7}$$

where H_{wick} is the wick height, $H_{\text{wick-max}}$ the maximum wick height, and τ the respond time. The maximum wick height of the heat pipes, however, shows a larger deviation, as the partially sintered powders or bead discontinuities due to unstable melt pool on the wall. From the test results, the heat pipes with fabricated by low power grooved-strategy has the best overall wick performance within the horizontal direction, while the heat pipe built by low power low
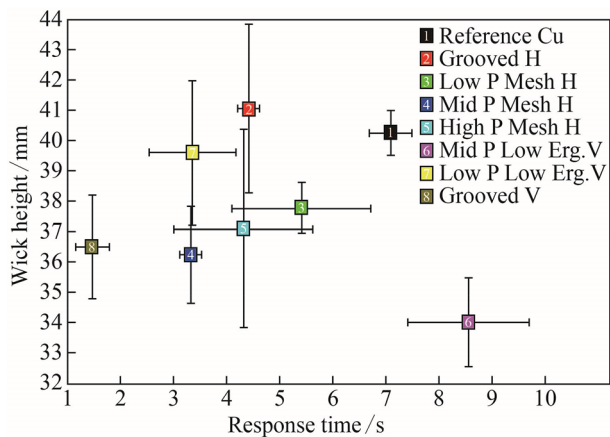
Fig. 13 Comparison of the response time and wick height of the LPBF heat pipes, with a Cu heat pipe as a reference

energy strategy (Low P Low Erg. V) has the best performance within the vertical direction. The grooved-strategy also showed a good performance within the vertical direction, as the response time was the shortest, yet the wicking height was slightly lower than the low energy scan strategy.

4 Conclusions and future work

Heat pipes with designed porosity structures have been successfully manufactured by adopting three different strategies (lower energy, mesh and grooved). The wick test results show the good performance of LPBFed heat pipes. The main conclusions are as follow.

(i) The relationship between laser input parameters (laser power and scan speed) and bead width of LPBF IN718 was concluded base on experimental results. The bead width logarithmically increases with the increase of linear energy density. The concluded equation can be applied to predict the melt pool width and the minimum feature size in LPBF IN718, which could be helpful for heat pipe design and manufacturing.

(ii) Heat pipes manufactured by LPBF, apart from medium power low energy sample, show better wick performance than sintered Cu heat pipe in wick test. The sintered/partial melt powder on the surface increases the surface area similar to a typical sintered wick structure. The grooved-strategy was able to produce heat pipes with good performance in both vertical and horizontal directions.

(iii) LPBF can produce thin wall or micro-channel structure around 100 μm width. The defects in the samples were caused by the unstable melt pool, which was mainly affected by the contact angle and space

between solids. The thin wall structure has a border processing range than the block structure due to round top surface.

(iv) The micro-CT can be used as a non-destructive evaluation method for the structural performance of LPB-Fed heat pipes. The micro-CT results suggested the structure produced by LPBF was stable under thermal cycles.

References

1. Jouhara H, Chauhan A, Nannou T et al (2017) Heat pipe based systems—advances and applications. Energy 128:729–754
2. Lee S, Lee J, Hwang H et al (2018) Layer-by-layer assembled carbon nanotube-polyethyleneimine coatings inside copper-sintered heat pipes for enhanced thermal performance. Carbon 140:521–532
3. Xiang J, Zheng H, Wang Y et al (2019) Numerical simulation, machining and testing of a phase change heat sink for high power LEDs. Materials 12(13):2193. https://doi.org/10.3390/ma12132193
4. Chan CW, Siqueiros E, Ling-Chin J et al (2015) Heat utilisation technologies: a critical review of heat pipes. Renew Sust Energ Rev 50:615–627
5. Brennan PJ, Kroliczek EJ (1979) Heat pipe design handbook: Volume II. NTIS, Publication no. N81-70113, Maryland, USA
6. Hoa C, Demolder BT, Alexandre A (2003) Roadmap for developing heat pipes for ALCATEL SPACE's satellites. Appl Therm Eng 23(9):1099–1108
7. Li H, Wang X, Liu Z et al (2015) Experimental investigation on the sintered wick of the anti-gravity loop-shaped heat pipe. Exp Therm Fluid Sci 68:689–696
8. Ngo TD, Kashani A, Imbalzano G et al (2018) Additive manufacturing (3D printing): a review of materials, methods, applications and challenges. Compos B Eng 143:172–196
9. Jared BH, Aguilo MA, Beghini LL et al (2017) Additive manufacturing: toward holistic design. Scr Mater 135:141–147

10. Parimi LL, Ravi GA, Clark D et al (2014) Microstructural and texture development in direct laser fabricated IN718. Mater Charact 89:102–111

11. Mazur M, Leary M, McMillan M et al (2017) Mechanical properties of Ti6Al4V and AlSi12Mg lattice structures manufactured by selective laser melting (SLM). Laser Additive Manufacturing, Woodhead Publishing, pp 119–161

12. Leary M, Mazur M, Elambasseril J et al (2016) Selective laser melting (SLM) of AlSi12Mg lattice structures. Mater Des 98:344–357

13. Qiu C, Yue S, Adkins NJE et al (2015) Influence of processing conditions on strut structure and compressive properties of cellular lattice structures fabricated by selective laser melting. Mat Sci Eng A 628:188–197

14. Huang Y, Xue Y, Wang X et al (2017) Effect of cross sectional shape of struts on the mechanical properties of aluminum based pyramidal lattice structures. MaterLett 202:55–58

15. Zhu S, Ma L, Wang B et al (2018) Lattice materials composed by curved struts exhibit adjustable macroscopic stress-strain curves. Mater Today Commun 14:273–281

16. Li S, Hassanin H, Attallah MM et al (2016) The development of TiNi-based negative Poisson's ratio structure using selective laser melting. Acta Mater 105:75–83

17. Essa HHK, Attallah MM, Adkins NJ et al (2017) Development and testing of an additively manufactured Monolithic catalyst bed for HTP thruster applications. Appl Catal A-Gen 542:125–135

18. Ameli M, Agnew B, Leung PS et al (2013) A novel method for manufacturing sintered aluminium heat pipes (SAHP). Appl Therm Eng 52(2):498–504

19. Ibrahim OT, Monroe JG, Thompson SM et al (2017) An investigation of a multi-layered oscillating heat pipe additively manufactured from Ti-6Al-4V powder. Int J Heat Mass Transf 108:1036–1047

20. Thompson SM, Aspin ZS, Shamsaei N et al (2015) Additive manufacturing of heat exchangers: a case study on a multi-layered Ti-6Al-4V oscillating heat pipe. Addit Manuf 8:163–174

21. Jafari D, Wits WW, Geurts BJ (2020) Phase change heat transfer characteristics of an additively manufactured wick for heat pipe applications. Appl Therm Eng 168:114890. https://doi.org/10.1016/j.applthermaleng.2019.114890

22. Tan C, Li S, Essa K et al (2019) Laser powder bed fusion of Ti-rich TiNi lattice structures: process optimisation, geometrical integrity, and phase transformations. Int J Mac Tool Manuf 141:19–29

23. Yadroitsev I, Gusarov A, Yadroitsava I et al (2010) Single track formation in selective laser melting of metal powders. J Mater Process Tech 210(12):1624–1631

24. Li C, Guo YB, Zhao JB (2017) Interfacial phenomena and characteristics between the deposited material and substrate in selective laser melting Inconel 625. J Mater Process Tech 243:269–281

25. Dilip JJS, Zhang S, Teng C et al (2017) Influence of processing parameters on the evolution of melt pool, porosity, and microstructures in Ti-6Al-4V alloy parts fabricated by selective laser melting. Prog Addit Manuf 2(3):157–167

26. Aydin S, Ali KY, Rashad S et al (2017) Three-dimensional microstructured lattices for oil sensing. Energy Fuels 31(3):2524–2529

27. Essa K, Sabouri A, Butt H et al (2018) Laser additive manufacturing of 3D meshes for optical applications. PLoS One 13(2):e0192389. https://doi.org/10.1371/journal.pone.0192389

28. Elsayed M, Ghazy M, Youssef YM et al (2018) Optimization of SLM process parameters for Ti6Al4V medical implants. Rapid Prototyp J 25(3):433–447

29. Valdez M, Kozuch C, Faierson EJ et al (2017) Induced porosity in super alloy 718 through the laser additive manufacturing process: microstructure and mechanical properties. J Alloys Compd 725:757–764

30. Salem H, Carter LN, Attallah MM et al (2019) Influence of processing parameters on internal porosity and types of defects formed in Ti6Al4V lattice structure fabricated by selective laser melting. Mat Sci Eng A 767:138387. https://doi.org/10.1016/j.msea.2019.138387

31. Liu Y, Zhang J, Pang Z (2018) Numerical and experimental investigation into the subsequent thermal cycling during selective laser melting of multi-layer 316L stainless steel. Opt Laser Technol 98:23–32

32. Searle M, Black J, Straub D et al (2020) Heat transfer coefficients of additively manufactured tubes with internal pin fins for supercritical carbon dioxide cycle recuperators. Appl Therm Eng 181:116030. https://doi.org/10.1016/j.applthermaleng.2020.116030

33. Zhang X, Tiwari R, Shooshtari AH et al (2018) An additively manufactured metallic manifold-microchannel heat exchanger for high temperature applications. Appl Therm Eng 143:899–908

34. Leung CLA, Marussi S, Atwood RC et al (2018) In situ X-ray imaging of defect and molten pool dynamics in laser additive manufacturing. Nat Commun 9(1):1355. https://doi.org/10.1038/s41467-018-03734-7

35. Bertoli US, Wolfer AJ, Matthews MJ et al (2017) On the limitations of volumetric energy density as a design parameter for selective laser melting. Mater Des 113:331–340

36. Suman B (2009) Microgrooved heat pipe. In: Irvine TF, Hartnett JP (eds) Advances in heat transfer. Elsevier, pp 1–80

37. Louvis E, Fox P, Sutcliffe CJ (2011) Selective laser melting of aluminium components. J Mater Process Tech 211(2):275–284

38. Johnson L, Mahmoudi M, Zhang B et al (2019) Assessing printability maps in additive manufacturing of metal alloys. Acta Mater 176:199–210

39. Kusuma C (2016) The effect of laser power and scan speed on melt pool characteristics of pure titanium and Ti-6Al-4V alloy for selective laser melting. Dissertation, Wright State University, p 128

40. Carter LN, Wang X, Read N et al (2016) Process optimisation of selective laser melting using energy density model for nickel based superalloys. Mater Sci Tech 32(7):657–661

41. Li R, Liu J, Shi Y et al (2012) Balling behavior of stainless steel and nickel powder during selective laser melting process. Int J Adv Manuf Tech 59(9):1025–1035

42. Bidare P, Bitharas I, Ward RM et al (2018) Fluid and particle dynamics in laser powder bed fusion. Acta Mater 142:107–120

43. Kong D, Zhang Y, Liu S (2019) Convective heat transfer enhancement by novel honeycomb-core in sandwich panel exchanger fabricated by additive manufacturing. Appl Therm Eng 163:114408. https://doi.org/10.1016/j.applthermaleng.2019.114408

44. Gu D, Yang Y, Xi L et al (2019) Laser absorption behavior of randomly packed powder-bed during selective laser melting of SiC and TiB_2 reinforced Al matrix composites. Opt Laser Technol 119:105600. https://doi.org/10.1016/j.optlastec.2019.105600

45. Boley CD, Khairallah SA, Rubenchik AM (2015) Calculation of laser absorption by metal powders in additive manufacturing. Appl Opt 54(9):2477–2482

46. Li Y, He HF, Zeng ZX (2013) Evaporation and condensation heat transfer in a heat pipe with a sintered-grooved composite wick. Appl Therm Eng 50(1):342–351

47. Jasper WJ, Anand N (2019) A generalized variational approach for predicting contact angles of sessile nano-droplets on both flat and curved surfaces. J Mol Liq 281:196–203
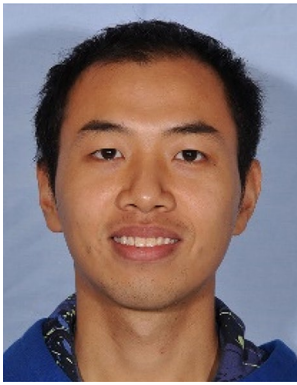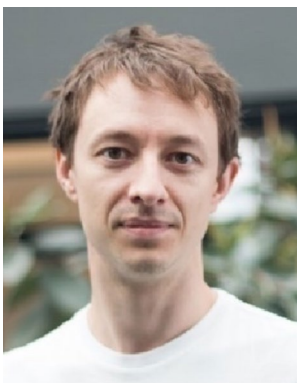
Sheng Li received Ph.D. degree in Materials Science from University of Birmingham, UK, in 2017. He is currently working as a research fellow in the School of Metallurgy and Materials, University of Birmingham. He is the author of 24 research publications. His research interests include additive manufacturing of metal and ceramic, processing and microstructure of shape memory alloys, Ni superalloys, Ti alloys, Al alloys and metal matrix composite. He has worked on the projects supported by leading companies across the world including Rolls-Royce, Airbus, Honda, BAE Systems, MBDA Missiles, MicroTurbo, Ford, and European Space Agency.

Khamis Essa is Reader in Advanced Manufacturing and Process Modelling at the School of Engineering, the University of Birmingham and the Director of the Advanced Manufacturing Group. His research is focused on advanced manufacturing technologies for instance Metal and ceramic 3D printing, Hot Isostatic Pressing and Incremental Sheet Forming. He has been developing novel manufacturing routes and applications for aerospace, defence, automotive and biomedical industries. The scientific emphasis of his research is on material and process interaction. He has been leading a number of research projects funded by EU, UK research councils and industry. His research has been supporting major companies across the world including Rolls-Royce, BAE Systems, MBDA Missiles, MicroTurbo, Ford, European Space Agency and Caterpillar. Dr Essa has over 80 journal and conference publications in addition to two patents and one book. He is guest editor for the micromechanics journal and is setting on the editorial board of three other international journals.

James Carr received his MPhys degree in 2008 and Ph.D. degree in Materials Science in 2014 from the University of Manchester. James Carr is an Applications Specialist for MicroCT at Blue Scientific. He acquired his first degree in Physics at the University of Manchester in 2008 and then a PhD in Materials Science in 2015. He has spent his research career specializing in 3D imaging and image processing at the Henry Moseley X-ray Imaging Facility and Diamond Light Source.

States Chiwanga received his BSc degree in Aeronautical Engineering from University of Salford, UK and his MSc degree in Fluid Mechanics from Washington State University, USA. States has worked in senior positions for well-known multinational engineering companies including Schlumberger, Solectron and PDD Group before starting Cambridge Engineering Analysis and Design Ltd. (CEAD) in 2007. He is now the director/CFD &Thermofluids Consultant in CEAD.

Andrew Norton received his MSci in Natural Sciences (Materials Science) from University of Cambridge and DPhil (Ph.D.) degree in Materials from University of Oxford, UK in 2013. He is now work as technologist and managing the projects gearfunded through Aerospace Technology Institute &InnovateUK, involving collaborations with a number of Rolls-Royce University Technology Centres and Small/Medium-Sized Enterprises, and utilise a global Research & Development supply chain network. Including the development of novel systems to perform inspection and repair inside aeroengines, emerging technologies (typically Technology Readiness Level 6 and below), supporting the movement of on-wing inspection and repair technologies into production through a wide ranging supply chain network.

Moataz M. Attallah holds a chair in advanced materials processing at the School of Metallurgy and Materials University of Birmingham. His research focuses on developing a metallurgical understanding of the material-process interaction in additive manufacturing of metallic materials focusing on the process impact on the microstructure and structural integrity development. His research is conducted through research partnerships with various companies in the aerospace, defence, medical, space, and nuclear energy sectors. He co-authored over 170 journal and conference papers, 3 book chapters, and is a co-inventor on 8 patent applications.